Acta Materialia 241 (2022) 118414

Contents lists available at ScienceDirect

Acta Materialia

journal homepage: www.elsevier.com/locate/actamat

# The effect of zirconium on the Ti-(42-46 at.%)Al system

Michael Musi[a,*], Stefan Kardos[a], Lukas Hatzenbichler[a], David Holec[a], Andreas Stark[b], Melissa Allen[c], Volker Güther[c], Helmut Clemens[a], Petra Spoerk-Erdely[a,*]

[a] Department of Materials Science, Montanuniversität Leoben, Franz Josef-Straße 18, Leoben 8700, Austria
[b] Institute of Materials Research, Helmholtz-Zentrum Hereon, Max-Planck-Straße 1, Geesthacht 21502, Germany
[c] GfE Metalle und Materialien GmbH, Höfener Straße 45, Nuremberg 90431, Germany

ARTICLE INFO

*Article history:*
Received 9 August 2022
Revised 23 September 2022
Accepted 30 September 2022
Available online 2 October 2022

*Keywords:*
Titanium aluminides
Phase transformations
*In situ*
Synchrotron diffraction
Ab initio calculations

ABSTRACT

In recent years, Zr has emerged as a promising alloying element for intermetallic $\gamma$-TiAl based alloys to improve their mechanical properties. The present work focuses on the influence of this element on the microstructure and the thermodynamic phase equilibria in the ternary Ti-(42-46)Al-(2-4)Zr (at.%) system. Alloying with Zr was found to increase the amount of the $\gamma$ phase in the microstructure of cast material densified by hot-isostatic pressing. Simultaneously, the material's hardness increased due to solid solution strengthening as well as the refinement of lamellae in the $\alpha_2/\gamma$ colonies. With respect to the phase transformation behaviour, a significant decrease of the solidus temperature was observed in the high Zr alloyed material variants. In combination with the stabilization of the $\gamma$ phase, this essentially results in a narrowing of the single $\alpha$ phase field region in the Ti-Al-Zr phase diagram derived in this work. *In situ* high-energy X-ray diffraction was performed on Ti-46Al-2Zr and Ti-46Al-4Zr (at.%) specimens to investigate the phase transitions above and below the solidus temperature by utilizing two different experimental setups. These experiments showed that upon heating, small amounts of $\beta$ phase are formed in both alloys prior to the transition into the peritectic $\alpha+\beta+$L phase field region. Furthermore, an additional heat treatment study was conducted to determine the influence of Zr and temperature on the resulting microstructure. The combination of X-ray diffraction techniques with ab-initio calculations revealed a significant asymmetric influence of Zr on the lattice parameter of the $\gamma$ phase, resulting in a decreasing $c/a$ ratio.



## 1. Introduction

Intermetallic $\gamma$-TiAl based alloys are an exceptional class of light-weight materials dedicated to high-temperature applications in the aeronautic and automotive industries [1,2]. Their low density of about 4 gcm$^{-3}$, combined with their high yield strength and creep resistance, result in excellent specific mechanical properties, which compare to competing material systems such as Ni-based alloys [2,3]. Within the Al range of modern engineering $\gamma$-TiAl based alloys, i.e. 42–48 at.% Al, several phases appear in the binary Ti-Al phase diagram depending on the temperature [2,4]. Cooling down from the liquid phase field region results in the nucleation of the first solid phase, the body-centred cubic $\beta$-Ti(Al) phase (A2 structure, *Im-3m*). Further solidification then proceeds either completely via this phase for Al contents below approximately 44.5 at.% or via a peritectic reaction of the $\beta$ and the liquid phase to the hexagonal $\alpha$-Ti(Al) phase (A3 structure, $P6_3/mmc$) for higher amounts of Al [4,5]. In the case of binary $\gamma$-TiAl based alloys, a single $\alpha$ phase field region is present over the whole Al range mentioned above [5]. Further cooling with intermediate or lower cooling rates results in the formation of the ordered tetragonal $\gamma$-TiAl phase ($L1_0$ structure, *P4/mmm*) and the ordering of the $\alpha$ phase into the hexagonal $\alpha_2$-$Ti_3Al$ phase ($D0_{19}$ structure, $P6_3/mmc$) at the eutectoid temperature [4,5].

In order to increase the service temperature of $\gamma$-TiAl based alloys and, thus, to conquer new application areas, a further improvement of their mechanical properties is a necessity. Especially, as the typical Al content of engineering $\gamma$-TiAl based alloys yields a significant amount of $\gamma$ phase in the microstructure, and as this phase governs most of the plastic deformation during mechanical loading, its strengthening is an essential part of the advancement of this material class [2,6]. Two important requirements for an efficient solid solution strengthening of the $\gamma$ phase are, firstly, a sufficiently high solubility of the alloying species and,

* Corresponding authors.
*E-mail addresses:* michael.musi@unileoben.ac.at (M. Musi), petra.spoerk-erdely@unileoben.ac.at (P. Spoerk-Erdely).

https://doi.org/10.1016/j.actamat.2022.118414

secondly, its preferred partition behaviour into this phase compared to co-existing phases. A promising candidate meeting both of these demands to improve the mechanical properties is Zr [7–9]. As demonstrated by Kainuma et al. [10] in a Ti-44Al-7.5Zr (at.%) alloy, this element partitions preferably into the $\gamma$ phase, followed by the $\beta$ phase, and least into the $\alpha$ phase below 1300°C. The solubility limit of Zr in the $\gamma$ phase was found to be 9 at.% at 1000°C [11], which increases to 11 at.% at both 1200°C and 1300°C [10]. Zirconium's solid solution strengthening effect is attributed to an asymmetric distortion of the $\gamma$ lattice structure with respect to the $a$ and $c$ axes [4]. Kawabata et al. [7] observed a decrease of the lattice parameters of the $\gamma$ phase for alloys based on the Ti-50Al (at.%) system when alloying with Zr, while the tetragonal distortion of $\gamma$ simultaneously increased. Contrarily, Tanda et al. [8] reported increasing lattice parameters and decreasing tetragonality for the same Al content. Similar behaviour was also reported for alloys containing 44 at.% of Al and 5 at.% of Zr [12,13]. Consequently, the effect of Zr on the lattice parameters and the tetragonality of the $\gamma$ phase is not unambiguously covered by the current literature.

With respect to the thermodynamic influence of Zr, a $\beta$-stabilizing effect as well as a full miscibility in the Ti-Zr system are mentioned in literature [14]. Contrarily, when alloyed to Al, Zr is found to form a variety of binary intermetallic phases [15]. In the case of the Ti-Al-Zr system, several studies reported on the absence of any ternary intermetallic phases [11,16–18]. Furthermore, a comparison of the isothermal sections of this ternary system also suggests a stabilization of the $\beta$ phase, while the existence regions of the $\alpha_2$, the $\alpha$ as well as the $\gamma$ phase seem to be reduced for Zr contents feasible in $\gamma$-TiAl based alloys [10,11,18]. In addition to studies of isothermal sections of the Ti-Al-Zr system, recent research work has also focused on the influence of Zr on the mechanical properties compared to other alloying elements [9,12,19]. However, a study dedicated to the effect of Zr on the phase transformations and corresponding transition temperatures in the composition range of advanced $\gamma$-TiAl based alloys by means of *in situ* techniques is still missing.

The current work presents a detailed investigation of the effect of Zr in six model alloys with systematically varied compositions based on the Ti-(42-46)Al-(2-4)Zr (at.%) system. The influence of Zr on the microstructure of the materials is shown, while differential scanning calorimetry (DSC) is employed to study the phase transformation behaviour. Special focus is laid on two model alloys with a nominal Al content of 46 at.%, i.e. a Ti-46Al-2Zr and a Ti-46Al-4Zr (at.%) alloy. As this specific Al content is situated in close proximity to the peritectic point involving the $\alpha$ and the $\beta$ phase in the Ti-Al system, *in situ* high-energy X-ray diffraction (HEXRD) and additional heat treatments were conducted for these selected alloys. The respective results provide insights into the phase transformation pathways and microstructural characteristics occurring at high temperatures, e.g. the melting of the materials and the corresponding features in the microstructure. Combining the results of DSC, HEXRD and heat treatments allows the assessment of two quasi-binary phase diagrams in terms of the Al content for 2 and 4 at.% of Zr, as well as the dependence on the Zr content itself. Furthermore, X-ray diffraction techniques are used to study the influence of both alloying elements and temperature on the lattice parameters of the $\gamma$ phase. These experimental findings are compared with theoretical data obtained by ab-initio calculations based on the density functional theory (DFT).

## 2. Experimental and computational methods

The present work investigates six different model alloys based on the Ti-(42-46)Al-(2-4)Zr (at.%) system. In accordance with their nominal chemical compositions, these alloys are designated Ti-42Al-2Zr, Ti-42Al-4Zr, Ti-44Al-2Zr, Ti-44Al-4Zr, Ti-46Al-2Zr, and Ti-46Al-4Zr, respectively. The exact chemical compositions of the alloys are summarized in Table 1. Chemical analysis was performed by X-ray fluorescence spectroscopy (Ti, Al), inductively coupled plasma optical emission spectroscopy (Zr, metallic impurities) and LECO combustion (gases). The material was provided by GfE Metalle und Materialien GmbH, Nuremberg, Germany. Alloys with a nominal Al content of 46 at.%, e.g. Ti-46Al-2Zr and Ti-46Al-4Zr, were produced by vacuum arc remelting (VAR) of compacted consumable electrodes consisting of Ti sponge, Al and Zr sponge, a following homogenization via induction skull melting, and centrifugal casting. A subsequent hot-isostatic pressing (HIP) at 1200°C for 4 h at 200 MPa was carried out to close residual casting porosity and increase the chemical homogeneity of the material [2]. The other four alloys were derived from these two alloys by additional alloying followed by four times VAR remelting into buttons. These buttons were subsequently subjected to a HIP treatment at 1150°C for 4 h at 110 MPa. Material in the as-HIPed condition was used for further heat treatments conducted in the course of this work.

**Table 1**
Chemical composition of the investigated alloys in the as-HIPed condition.

| Alloy | Ti [at.%] | Al [at.%] | Zr [at.%] | O [m.-ppm] |
|---|---|---|---|---|
| Ti-42Al-2Zr | 55.3 | 42.4 | 1.9 | 800 |
| Ti-42Al-4Zr | 53.1 | 42.3 | 4.1 | 840 |
| Ti-44Al-2Zr | 53.6 | 44.0 | 2.0 | 1000 |
| Ti-44Al-4Zr | 50.8 | 44.4 | 4.3 | 1300 |
| Ti-46Al-2Zr | 51.2 | 46.5 | 2.1 | 510 |
| Ti-46Al-4Zr | 49.2 | 46.3 | 4.4 | 400 |

DSC measurements performed on a LabSys Evo by Seteram, France, were utilized to determine the phase transition temperatures of the alloys. Cylindrical samples with an average mass of 80 mg were heated in $Al_2O_3$ crucibles sealed by $Al_2O_3$ caps in a He5.0 atmosphere at three different heating rates, i.e. 10, 20 and 40°C/min. An extrapolation of the transition temperatures for these heating rates to a heating rate of 0°C/min yielded the phase transformation temperatures close to thermodynamic equilibrium. A blank measurement with an empty crucible was performed prior to each experiment and was subtracted from the experimental data.

*In situ* HEXRD experiments were conducted on samples of the Ti-46Al-2Zr alloy and the Ti-46Al-4Zr alloy at the Hereon-operated beamline P07 at the storage ring PETRA III at the Deutsches Elektronen-Synchrotron (DESY), Hamburg, Germany. Two different types of *in situ* experiments were performed, which are designated as "heating" and "melting" experiments, respectively. Both experiments were carried out within a modified DIL805A/D dilatometer from TA Instruments, Germany, in which the sample is inductively heated in a high-purity Ar6.0 atmosphere [20]. The *in situ* heating experiments consisted of a short annealing segment at 1000°C for 15 min followed by a first heating segment up to 1200°C with 2°C/min and a second heating segment up to the material's solidus temperature with 20°C/min. The samples possessed a cylindrical shape with a diameter of 5 mm and a length of 10 mm. For these experiments, the thermocouple of type S used for temperature control was attached to the sample with only a 200 µm thick Ta foil in between. This foil served the purpose of a diffusion barrier between the thermocouple and the sample material. While this experimental setup of the *in situ* heating experiments is excellent to investigate solid-solid phase transformations, it fails for phase transformations involving the liquid phase due to detachment of the needed Ta foil, resulting in incorrect temperature readings or experimental failure. Consequently, a second type of experiments, i.e. the *in situ* melting experiments, was introduced to shed light on the solid-liquid transformations. For these measurements, sam-

ple material was encapsulated in a hollow Mo cylinder with an inner diameter of 5 mm and a wall thickness of 300 µm and sealed by Mo caps. The Mo cylinder acted as the attachment point for the type S thermocouple, thus, preventing detachment even when the liquid phase was present. For more details regarding this type of *in situ* HEXRD experiments, the reader is referred to Ref. [21]. During the *in situ* melting experiments, the samples were heated from 1200°C up to temperatures situated in the $\beta$+L phase field region employing a heating rate of 20°C/min.

The mean photon energy of the *in situ* heating and *in situ* melting HEXRD experiments was 87.1 keV and 73.9 keV, respectively, and a beam cross-section of 1 × 1 $mm^2$ was used in both cases. A Perkin Elmer XRD 1621 area detector, placed approximately 1.5 m behind the sample, was used to capture the diffraction signal during the experiments. The diffraction setup, e.g. the exact sample-detector distance, was calibrated with $LaB_6$ powder. The azimuthal integration of the 2D diffraction data was performed with the software FIT2D [22]. The software MAUD was used to determine the volume fractions and the lattice parameters of the individual phases as a function of temperature via sequential Rietveld analysis of the integrated diffraction data [23].

Heat treatments at 1325°C and above were performed in a calibrated high-temperature furnace of type RHF 1600 from Carbolite, Germany, to verify the results of the DSC and *in situ* HEXRD measurements of the Ti-46Al-2Zr and the Ti-46Al-4Zr alloy. The exact heat treatment times and temperatures are given in Section 3.3. The cuboid samples with the dimensions 8 × 8 × 8 $mm^3$ were water-quenched after the heat treatments in order to preserve the high-temperature microstructures. The microstructural characterization of the as-HIPed and the heat-treated material was conducted with a scanning electron microscope (SEM) of type CLARA from Tescan, Czech Republic, using the back-scattered electron (BSE) contrast. X-ray diffraction (XRD) was performed using an AXS D8 Advance diffractometer from Bruker, USA. Prior to the characterization, the samples were prepared according to the procedure described in Ref. [24]. A further characterization of selected sample conditions was performed by energy dispersive X-ray spectroscopy (EDS) as well as electron back-scatter diffraction (EBSD). EDS was performed in the aforementioned SEM device operating at an acceleration voltage of 20 kV using an 80 $mm^2$ X-max detector and the software Aztec, both from Oxford Instruments, United Kingdom. The EBSD measurements were conducted on a field emission device Versa 3D Dual Beam from Thermo Fischer, USA, utilizing a Hikari XP EBSD camera together with the software TEAM and OIM for data acquisition and evaluation, all from EDAX, USA. TEM investigations of electrolytically prepared thin foils of the Ti-46Al-2Zr and the Ti-46Al-4Zr alloy were conducted on a CM12 from Philips, Netherlands, operating at 120 kV to determine the average lamellae spacing. Additionally, hardness measurements of HIP material were performed on a Qness Q60A+ measuring device equipped with a Vickers indenter tip. Ten individual HV10 measurements were conducted for each sample.

Ab-initio calculations were carried out by using the density functional theory [25,26] as implemented in the Vienna Ab-initio Simulation Package (VASP) to study the influence of Zr on the lattice parameters of the $\gamma$ phase [27,28]. The electron-ion interactions were described with projector augmented wave (PAW) pseudopotentials [29], exchange and correlation effects were treated at generalized gradient approximation level as parametrized by Perdew, Burke and Ernzerhof (GGA-PBE) [30]. To ensure the accuracy of 1 meV/atom or better, a plane-wave cut-off energy (ENCUT) of 500 eV was used for all the calculations. A 6 × 6 × 6 Γ-centred Monkhorst-Pack k-point mesh was generated automatically to sample the irreducible Brillouin zone. 3 × 3 × 3 supercells (108 atoms) were generated via a special quasi-random structure (SQS) generator [31] from the fully relaxed and tetragonally distorted $L1_0$ structure of the $\gamma$ phase. Simultaneously, the desired amount of Zr atoms was distributed on the Ti sublattice and the excess Ti atoms were placed on the Al sublattice. Amounts of Zr atoms were chosen so that the chemical constitution of the calculations corresponded to the investigated composition range of the model alloys. After relaxation of the supercell volumes, shapes and atomic positions, the optimized lattice parameters were extracted from the compositionally varying structures.

## 3. Results and discussion

### 3.1. Initial condition

The microstructures of the alloys in the as-HIPed condition, which acted as the initial state for further experiments, are shown in Fig. 1a-f. A comparison of the individual micrographs shows that the microstructures bear a strong resemblance to each other, i.e. they all consist of lamellar $\alpha_2/\gamma$ colonies and globular $\gamma$ phase. Respective examples of these microstructural features are marked in Fig. 1 by white arrows. Upon closer examination, an increased amount of globular $\gamma$ phase is observed for the alloys with a higher Al content. An increased amount of Al shifts the phase equilibrium between the $\alpha/\alpha_2$ and the $\gamma$ phase in favour of the latter one for all temperatures at which both phases are stable [5]. As the amount of $\gamma$ phase present at the HIP temperature corresponds primarily to the globular $\gamma$ phase in the final microstructure [2], an increased fraction of this microstructural feature is observed for higher Al contents. The $\alpha_2/\gamma$ colonies emerge during the cooling at the end of the HIP processing due to the formation of $\gamma$ lamellae and the ordering of $\alpha$ into $\alpha_2$ at the eutectoid temperature [2,4].

In the alloys with the highest Al content, i.e. Ti-46Al-2Zr and Ti-46Al-4Zr, local chemical segregations can be seen in the respective microstructures (Fig. 1c and f), while none of these are present in the other alloys. These segregations consist solely of globular $\gamma$ phase, and EDX measurements revealed a slightly higher Zr content when compared to the remaining microstructure, which causes the brighter BSE contrast in Fig. 1. As these local Zr enrichments must be remnants of the casting process, they indicate a different solidification behaviour of the Ti-46Al-xZr alloys compared to the other alloys with lower Al contents. Generally, casting segregations are observed in peritectically solidifying $\gamma$-TiAl based alloys, while a solidification completely via the $\beta$ phase typically results in a microstructure almost free of any macroscopic segregations [4,32]. Although a HIP treatment was conducted after casting, these Zr enrichments could not be eliminated in the Ti-46Al-2Zr and Ti-46Al-4Zr alloy. This is attributed to the fact that the HIP temperature of 1200 °C is situated within the two-phase $\alpha+\gamma$ phase field region, thus, prohibiting large-scale chemical equilibration across the phase boundaries. Furthermore, as indicated by the BSE contrast difference within this globular $\gamma$ phase situated at these Zr enrichments, the portion already present at the HIP temperature acted as a nucleation site for forming additional $\gamma$ phase during cooling. Since Zr is a large atom when compared to Ti and Al, e.g. the atomic radii of Zr, Ti and Al are 155 pm, 140 pm and 125 pm [33], respectively, the diffusion of Zr in the $\gamma$-TiAl phase can be expected to be lower than the Ti and Al self-diffusion and, thus, the resulting Zr difference within this globular $\gamma$ phase cannot be fully eliminated during the cooling segment of the HIP treatment [34,35]. However, the quantitative difference in the Zr content was found to be minor and, consequently, such local Zr enrichments were eliminated during subsequent heat treatments conducted at higher temperatures.

A comparison of the HIP microstructures with respect to the Zr content indicates that for the lower Zr content of 2 at.% (Fig. 1a-c) the amount of $\alpha_2$ phase is higher than in the alloys with the higher Zr content of 4 at.% (Fig. 1d-f). Consequently, XRD measure-

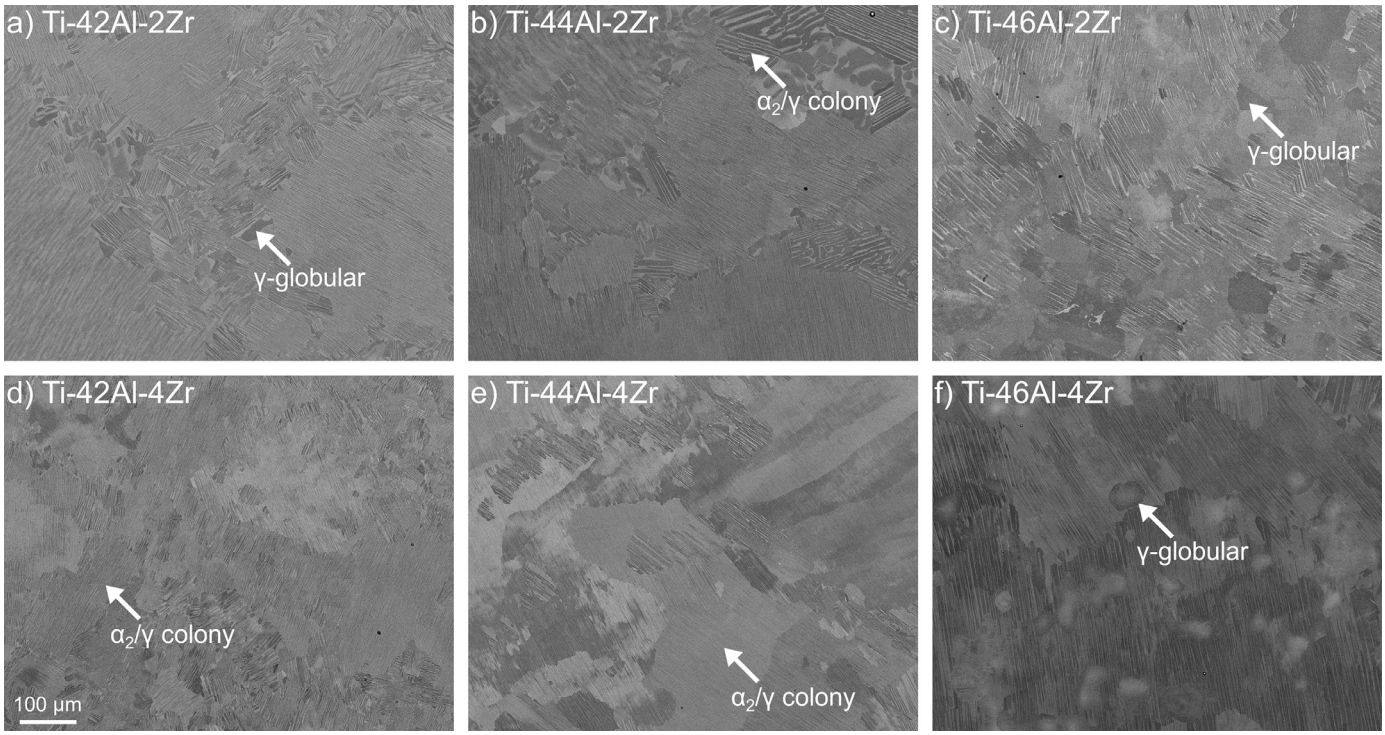


**Fig. 1.** SEM micrographs of the investigated alloys taken in BSE mode after the HIP treatment. Examples of the predominant microstructural features, i.e. the $\alpha_2/\gamma$ colonies as well as the globular $\gamma$ phase, are marked by white arrows. The $\alpha_2$ phase exhibits a light contrast and the $\gamma$ phase a dark contrast. The brighter zones in (f) corresponds to local Zr enrichment in the $\gamma$ phase (see text).

**Table 2**
Phase fractions determined by XRD and HV10 hardness of the investigated alloys in the as-HIPed condition.

| Alloy | $\alpha_2$ fraction [vol.%] | $\gamma$ fraction [vol.%] | Hardness [HV10] |
|---|---|---|---|
| Ti-42Al-2Zr | 30.4 | 69.6 | 333 ± 16 |
| Ti-42Al-4Zr | 25.9 | 74.1 | 352 ± 22 |
| Ti-44Al-2Zr | 19.3 | 80.7 | 314 ± 20 |
| Ti-44Al-4Zr | 14.2 | 85.8 | 359 ± 14 |
| Ti-46Al-2Zr | 12.8 | 87.2 | 275 ± 5 |
| Ti-46Al-4Zr | 8.6 | 91.4 | 296 ± 7 |

ments of the alloys in the as-HIPed condition were performed to quantify this observation. The resulting volume fractions of the $\alpha_2$ and the $\gamma$ phase are given in Table 2. Both Al and Zr are found to increase the amount of $\gamma$ phase at the expense of the $\alpha_2$ phase. With respect to the mean quantitative effect of these two alloying elements on the stabilization of the $\gamma$ phase in the investigated composition range, it can be said that the addition of 1 at.% Zr changes the amount of $\gamma$ phase by approximately 2.3 vol.%, while it is 4.4 vol.% in the case of 1 at.% Al. Consequently, the potential of Zr as a $\gamma$-stabilizing alloying element is approximately only half of that of Al. A qualitatively similar stabilization of the $\gamma$ phase over the $\alpha_2$ phase was also reported in a recent work by Imayev et al. [9], who compared the appearing phases in forged and heat-treated Ti-44Al-0.2B and Ti-44Al-5Zr-0.2B (at.%) alloys. Furthermore, in agreement with the respective isothermal sections of the ternary Ti-Al-Zr system available in literature [10,11,18], the XRD measurements and the microstructural images presented in Fig. 1 show no indications of any phase unrelated to the binary Ti-Al system.

The hardness of the alloys in the as-HIPed condition is shown in Table 2. Statistical analysis reveals that Al decreases the material's hardness, while Zr is found to increase it regardless of the Al content. The decrease in hardness due to Al can be explained by the fact that Al mainly tends to increase the amount of $\gamma$ phase, which is considered the softest phase in $\gamma$-TiAl based alloys [4,5,36,37]. Although Zr also increases the amount of $\gamma$ phase, it additionally provides, in contrast to Al, a solid solution strengthening of the material, thus counteracting the softening caused by the increased $\gamma$ phase fraction. Exemplarily, this solid solution strengthening was reported in literature by Tanda et al. [8], who observed a significant increase in hardness and strength in single $\gamma$ phase Ti-Al-Zr alloys for increased Zr contents. As a significant part of the microstructure consists of lamellar $\alpha_2/\gamma$ colonies, changes in the lamellar spacing could potentially also have a significant influence on the material's hardness [4]. Therefore, TEM investigations were conducted on the Ti-46Al-2Zr and the Ti-46Al-4Zr alloys to determine the average spacing of the lamellae inside the $\alpha_2/\gamma$ colonies. In agreement with the work of Bresler et al. [19], a decreasing lamellar spacing from 580 ± 89 nm for the Ti-46Al-2Zr alloy to 313 ± 41 nm for the Ti-46Al-4Zr alloy was observed. Consequently, the hardness increase due to the Zr additions in the present work can be attributed to solid solution strengthening as well as to a decreased lamellar spacing.

### 3.2. Phase transformation behaviour

DSC measurements were conducted to investigate the effect of Zr on the phase transformation behaviour over a large range of different Al contents. The heat flow curves corresponding to measurements with a heating rate of 20°C/min are shown in Fig. 2. Note that the individual curves have been shifted along the ordinate for a better visibility. Depending on temperature and alloy composition, several distinct peaks corresponding to different phase transformations are observable. An example for each of the occurring phase transformations is marked by an individual number above the respective peak in Fig. 2. For the exact values of the phase transformation temperatures determined by DSC, the reader is re-

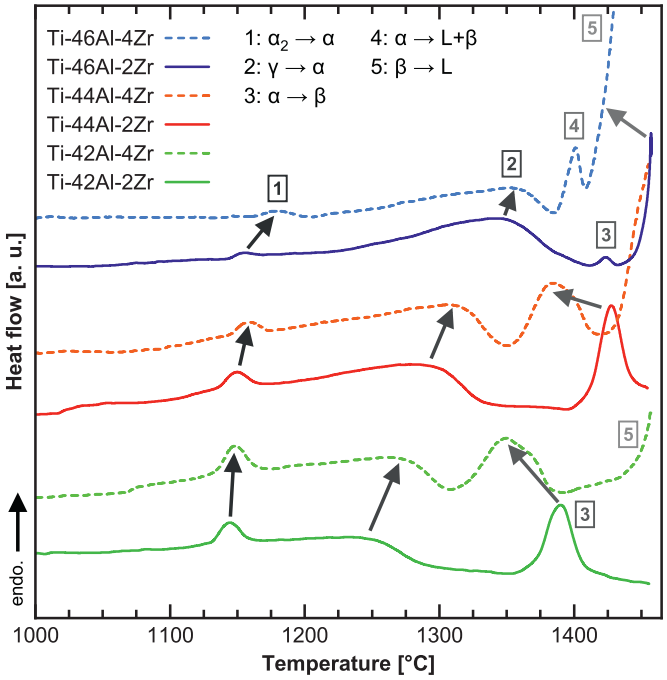


**Fig. 2.** Heat flow curves obtained from DSC measurements conducted with a heating rate of 20°C/min. The line colour indicates the Al content, while solid lines and dashed lines correspond to 2 at.% or 4 at.% Zr, respectively. Peaks associated with different phase transformations are exemplarily marked by individual numbers.

ferred to Table A.1 in the appendix. The effect of Zr on the different peaks is visualized by arrows. Starting from low temperatures, the first peak between 1100 °C and 1200 °C marks the disordering of the $\alpha_2$ phase into the $\alpha$ phase at the eutectoid temperature upon heating. In the binary Ti-Al system, the eutectoid temperature is independent of the Al content and occurs always at 1120 °C [5]. However, this has not to be the case in ternary Ti-Al-X systems, because the eutectoid line is morphed into a three-phase $\alpha+\alpha_2+\gamma$ phase field region. In the present study, both Al and Zr are found to increase the eutectoid temperature, with Zr exhibiting a stronger effect at a higher Al content. Furthermore, the area under a peak in the DSC curve is proportional to the reaction enthalpy of the associated phase transformation and the amount of transformed phase [38]. Consequently, the decreasing areas of the eutectoid peaks due to Al and Zr additions predict a decreased amount of $\alpha_2$ phase transforming into $\alpha$ phase. Thus, the trends observed in Section 3.1, i.e. the phase fractions determined by XRD, are confirmed.

The next peak encountered during further heating, which partially overlaps with the eutectoid peak, corresponds to transformation of the $\gamma$ phase into the $\alpha$ phase. The $\gamma$-solvus temperature, which marks the end temperature of this transformation, at which the $\gamma$ phase has completely dissolved, is associated with the maximum temperature of this peak. Similar to the eutectoid peak, the $\gamma$-solvus peak is also shifted to higher temperatures when increasing the concentration of Al and Zr in the material. However, a discussion of the peak area is difficult in this case, because the offsets of these peaks overlap with other phase transformations for most of the investigated alloys, thus, making an exact peak area determination impossible.

In contrast to the behaviour of the eutectoid and the $\gamma$-solvus peak described above, quite an opposite trend can be found for the phase transformations at higher temperatures. In the Ti-42Al-2Zr alloy (green solid line in Fig. 2), an extensive single $\alpha$ phase field region occurs above the $\gamma$-solvus temperature, as indicated by the large region with a nearly horizontal heat flow curve between 1275 °C and 1350 °C. The following peak (#3 in Fig. 2) marks the transformation of the $\alpha$ phase into the $\beta$ phase. In the corresponding alloy variant with 4 at.% Zr (green dashed line in Fig. 2), this peak is shifted to lower temperatures. Furthermore, on the very right of Fig. 2 at the highest temperature, the beginning of the melting process, i.e. the $\beta \rightarrow$L transformation, can be seen for this particular alloy (peak #5). In accordance with the binary Ti-Al phase diagram, the higher Al content of the Ti-44Al-2Zr alloy (red solid line in Fig. 2) shifts the $\alpha \rightarrow \beta$ phase transformation to higher temperatures [5]. For the Ti-44Al-4Zr alloy, the respective peak occurs again at lower temperatures. Additionally, the peak associated with the $\beta \rightarrow$L transformation is shifted to lower temperatures, also when compared to the Al-lean alloy variants. This phase transformation behaviour is in agreement with the observed microstructural homogeneity for the Ti-42Al-xZr and the Ti-44Al-xZr alloys discussed in Section 3.1, which suggested a complete solidification via the $\beta$ phase.

With respect to the alloys containing 46 at.% Al, the transformation behaviour at high temperatures, i.e. the melting of the material, is of particular interest. As described in Section 3.1, the microstructure of these alloys contains local enrichments in Zr, which are indicative of a peritectic solidification. When compared to the binary Ti-Al system, an Al content of 46 at.% lies close to the peritectic point, at which material would transition from a single $\alpha$ phase field region directly into the $\beta$+L phase field region [5]. Considering the influence of Zr in the ternary system, three potential transformation pathways are conceivable in the proximity of this peritectic point upon heating, when starting from the $\alpha$ phase field region. Firstly, the material could behave as described above and transition directly into the $\alpha+\beta$+L phase field region. Secondly, a limited amount of $\beta$ phase could form prior to entering this three-phase field region, essentially corresponding to a composition on the Al-lean side of the peritectic point in the related Ti-Al-Zr phase diagram. The last option is to proceed through an $\alpha$+L phase field region at the Al-rich side of the peritectic point. Upon a closer inspection of the DSC curves of the Ti-46Al-2Zr and the Ti-46Al-4Zr alloy (solid and dashed blue lines in Fig. 2), quite different behaviours can be observed. In the first case, a small peak occurs at the beginning of the peak associated with the melting of the material. As transformations involving the liquid phase usually possess higher reaction enthalpies than solid-solid phase transformations [39], this small peak may be attributed to the formation of $\beta$ phase rather than the liquid phase. In the case of the Ti-46Al-4Zr alloy, the $\gamma$-solvus peak is followed by two large peaks (#4 and #5 in Fig. 2). Taking into account that only a limited amount of $\beta$ phase may form for this alloy's Al content, and that the relative area of peak #4 is comparable to those of the $\beta \rightarrow \alpha$ peaks of the Al-leaner alloys, it may be associated to a phase transformation involving the liquid phase. Thus, this peak probably corresponds to the $\alpha \rightarrow \beta$+L peritectic reaction. The peak at higher temperatures should therefore mark the $\beta \rightarrow$L transformation.

Generally, it is difficult to verify the presence of small amounts of phases by DSC, especially when the respective transformation is overlapping with other phase transitions. A powerful technique that allows the observation of even the smallest amounts of phases (<1 vol.%) in the Ti-Al system is HEXRD [40]. Consequently, *in situ* HEXRD experiments were conducted for the Ti-46Al-2Zr and the Ti-46Al-4Zr alloy to clarify the phase transformation behaviour at high temperatures and to complementarily assess the transition temperatures. In order to investigate the phase evolution below the solidus temperature of the respective alloy, *in situ* heating experiments were performed, during which the thermocouple was attached to the sample via a thin Ta foil. For similar experiments on other alloy systems the reader is referred to Refs. [41–43].

Taking into account the excellent signal-to-noise ratio of HEXRD utilizing synchrotron radiation [40], the *in situ* heating HEXRD

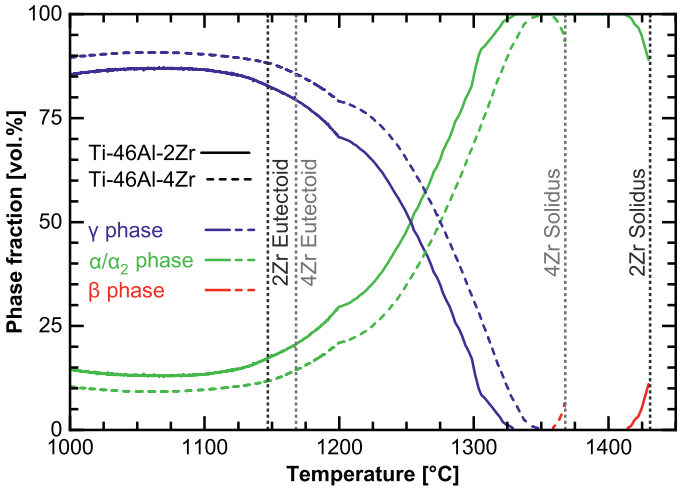


**Fig. 3.** Evolution of the volume fraction of the $\alpha/\alpha_2$ (green), $\beta$ (red) and $\gamma$ (blue) phase during the *in situ* heating HEXRD experiments conducted on Ti-46Al-2Zr (solid lines) and Ti-46Al-4Zr (dashed lines). In addition, the eutectoid and solidus temperatures of the alloys determined by the *in situ* heating and *in situ* melting experiments, respectively, are shown.

measurements confirm that the microstructures of the alloys consist of only two phases below the eutectoid temperature, i.e. the $\alpha_2$ phase and the $\gamma$ phase, in accordance with the XRD measurements. The volume fraction evolution of these phases in the Ti-46Al-2Zr and the Ti-46Al-4Zr alloy upon heating below the solidus temperature is depicted in Fig. 3. A comparison of the phase fractions of the individual alloys at 1000°C with the as-HIPed condition in Section 3.1 shows a good quantitative agreement. Starting from 1000°C with a heating rate of 2°C/min, only slight changes of the volume fractions are observable up to 1100°C. Note that, while the volume fractions of the low-temperature $\alpha_2$ phase and the high-temperature $\alpha$ phase are shown in Fig. 3 as one curve, a discrimination between these two phases is possible by HEXRD due to the vanishing of the related superstructure peaks of the $\alpha_2$ phase upon heating. The disordering temperatures, i.e. the eutectoid temperatures, are 1148°C and 1167°C for the Ti-46Al-2Zr and the Ti-46Al-4Zr alloy, respectively.

The discontinuous change of the slope at 1200°C is attributed to a change of the heating rate from 2°C/min to 20°C/min to limit extensive grain growth, which deteriorates the HEXRD signal once a single phase field region is encountered. Further heating results in the complete transformation of the $\gamma$ phase into the $\alpha$ phase. In case of the Ti-46Al-2Zr alloy, the dissolution of the $\gamma$ phase at a $\gamma$-solvus temperature of 1331°C occurs at a lower temperature than in the alloy with the higher Zr content. In both alloys, an $\alpha$ phase field region is encountered above the $\gamma$-solvus temperature. Additionally, before the solidus temperature of the individual alloys is reached, a certain amount of $\beta$ phase is observed in the *in situ* heating experiments. For the Ti-46Al-2Zr alloy, this formation of the high-temperature $\beta$ phase could be predicted from the corresponding DSC curve shown in Fig. 2. Contrarily, for the Ti-46Al-4Zr alloy, this was not evident from the DSC measurement. The reason for this is that the $\alpha$ phase field region is rather small for this alloy variant, as it only spans around 10°C. Consequently, the $\beta$ formation peak disappears under the $\gamma$-solvus and peritectic peak due to its significantly smaller intensity, e.g. compare peak #3 with peaks #2 and 4 in Fig. 2. The presence of $\beta$ phase below the solidus temperature finally provides evidence that both alloys with 46 at.% Al are situated at the Al-lean side of the peritectic point.

The second type of *in situ* HEXRD experiments, the *in situ* melting experiments, was used to investigate the phase transformation behaviour of the Ti-46Al-2Zr and the Ti-46Al-4Zr alloy at temperatures above their respective solidus temperatures. The experimental setup of the *in situ* heating experiments does not allow reliable measurements above the solidus temperatures of the alloys due to detachment of the thermocouple used for temperature control. The detachment is caused by extensive reactions with the formed liquid phase, which yields incorrect temperature readings and failure of the experiment. As a result, for the *in situ* melting experiments, the material is rather placed in a special sample holder made of Mo consisting of a hollow tube sealed off by caps. On the one hand, this sample holder contains the melting material and, on the other hand, it allows to safely attach the thermocouple.

Selected HEXRD spectra taken from the *in situ* melting experiment of the Ti-46Al-4Zr alloy at different temperatures are shown in Fig. 4a. The spectra belonging to this alloy were chosen because of the superior signal quality compared to ones of the low Zr variant, which experienced significant grain growth due to the relatively large single $\alpha$ phase field region. In Fig. 4a, the peaks corresponding to the observed phases are marked by individual symbols. However, in addition to the peaks associated with the phases occurring in the Ti-Al system, some further peaks belong to the sample holder made of Mo possessing a body-centred cubic crystal structure. In agreement with the *in situ* heating experiments of both alloys, the $\alpha$ and $\beta$ phase are stable below the solidus temperature of 1366°C, see black spectrum in Fig. 4a. The $\alpha+\beta$ HEXRD spectrum taken at 1365°C is plotted again in the form of a grey dashed line in Fig. 4a as a reference for the other two spectra taken at higher temperatures to highlight the occurrence of the liquid phase. Although this latter phase possesses no periodic long-range structure, it contributes to the HEXRD signal. Precisely, the formation of liquid phase is accompanied by the occurrence of a broad amorphous peak approximately centred at a diffraction angle of 4.2°. This peak is most obvious in the $\beta$+L spectrum (violet line in Fig. 4a), which is characterized by a high amount of liquid phase in comparison to the other spectra. For the $\alpha+\beta$+L spectrum (blue line in Fig. 4a), first signs of the peak of the liquid phase can be spotted at around 4.0°, a diffraction angle at which it does not overlap with the peaks of neither the $\alpha$ nor the $\beta$ phase.

The evolution of the $\alpha$, $\beta$ and liquid phase upon heating can be directly visualized by tracing the evolution of the relative intensity of one selected peak of each phase. The corresponding curves are shown in Fig. 4b and c for the Ti-46Al-2Zr and the Ti-46Al-4Zr alloy, respectively. For the $\alpha$ and the $\beta$ phase, the $\alpha$-102 and $\beta$-200 peaks were used, because these peaks do not overlap with the peaks of the liquid phase and the Mo sample holder. With respect to the liquid phase, the peak intensity was determined after subtraction of the reference curve, i.e. the HEXRD spectrum just before the solidus temperature is reached. This subtraction is necessary, because a diffusive background, arising from the synchrotron radiation itself, is present regardless of the temperature in the same Bragg angle region. For a better comparison, the determined peak intensities were normalized with the respective maximum value observed in the investigated temperature range.

In the case of the Ti-46Al-2Zr alloy (Fig. 4b), the transition through the $\alpha+\beta$ phase field region results in a decreasing $\alpha$ peak and an increasing $\beta$ peak intensity due to respective changes of the phase fractions below the solidus temperature. Once this temperature is reached at 1430°C, a significant increase in the $\beta$ and liquid peak intensity at the expense of the $\alpha$ peak is observed, caused by the $\alpha\rightarrow\beta$+L phase transformation. The dissolution temperature of the $\alpha$ phase coincides with a maximum in the relative intensity of the $\beta$-200 peak, as the material enters the $\beta$+L phase field region and transitions, upon further heating, towards the alloy's liquidus temperature. It is evident from Fig. 4c that a qualitatively similar phase evolution occurs in the Ti-46Al-4Zr alloy. However, the respective phase transformations are shifted to significantly lower temperatures due to the higher Zr content.

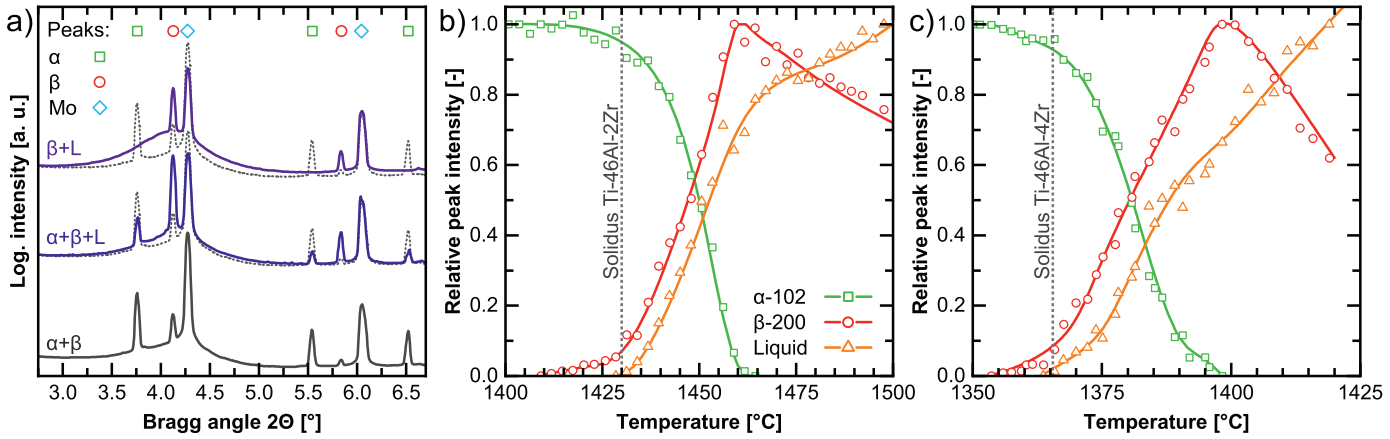


**Fig. 4.** (a) Selected diffraction spectra obtained during the *in situ* melting experiment of the Ti-46Al-4Zr alloy at temperatures within the $\alpha+\beta$ (1365°C), the $\alpha+\beta+$L (1385°C) and the $\beta+$L phase field region (1410°C), respectively. The grey dotted reference curves are used to highlight the broad peak associated with the liquid phase and correspond to the $\alpha+\beta$ HEXRD spectrum. Additionally, the peaks of the different phases are marked by individual symbols; (b) and (c) show the relative intensity evolution of the $\alpha$-102, $\beta$-200 and the liquid peak in the Ti-46Al-2Zr and the Ti-46Al-4Zr alloy (see text).

The findings of both types of HEXRD experiments are valuable additions to the DSC results, providing evidence for the phase transformation pathways of the alloys and, especially, for the presence of $\beta$ at temperatures below the $\alpha+\beta+$L phase field region. However, due to small amount of $\beta$ phase formed, the corresponding $\alpha\rightarrow\beta$ peak vanishes under the peaks of the other phase transformations in the DSC curve of the Ti-46Al-4Zr alloy in Fig. 2. Ultimately, the respective transition temperatures are all in good agreement with the DSC results, e.g. see Table A.1 in the Appendix.

### *3.3. Microstructural evolution during high-temperature heat treatments*

Heat treatments were performed to verify the results of the HEXRD and DSC measurements and to exclude any effects of phase transformation kinetics on the obtained findings. A preliminary study was conducted to determine the necessary heat treatment time to allow the occurring phase transformations to be properly completed. In particular, XRD and SEM investigations of samples of the Ti-46Al-2Zr and Ti-46Al-4Zr alloy heat-treated at 1325°C for various holding times followed by water-quenching revealed that no significant changes with respect to the phase fractions and the microstructural appearance occurred between 30 min and 1 h. Consequently, for heat treatments at higher temperatures, a holding time of 30 min is sufficient to bring the material as close to thermodynamic equilibrium as possible within the measurement uncertainties of the applied experimental techniques.

The microstructures of the Ti-46Al-2Zr and the Ti-46Al-4Zr alloys after heat treatments at different temperatures followed by water-quenching are presented in Fig. 5. A heat treatment at 1325°C for 1 h (Fig. 5a and b) yields a microstructure for both materials consisting of $\alpha_2$ phase and $\gamma$ phase. More specifically, the $\gamma$ phase occurs in either lamellar or globular shape. The $\gamma$ lamellae are remnants of the $\alpha_2/\gamma$ colonies in the HIP microstructure (see Fig. 1c and f). Due to the relatively high Al content of these alloys, the $\alpha$ phase is partially metastable during water-quenching and, thus, transforms into massive $\gamma$ phase. This massive $\gamma$ phase is characterized by a feathery appearance, e.g. marked with an arrow in Fig. 5a [2]. However, its distinct microstructural appearance allows an easy distinction from the $\gamma$ phase already present at the heat treatment temperature before water-quenching. Additionally, the ordering of $\alpha$ into $\alpha_2$ cannot be prevented, either, during water-quenching [44]. The presence of both the $\alpha$ phase and the $\gamma$ phase at 1325°C is in agreement with the findings of the HEXRD and DSC measurements, which predict an $\alpha+\gamma$ phase field region for said temperature. The heat treatment temperatures for Fig. 5c and d, 1375°C for Ti-46Al-2Zr and 1350°C for Ti-46Al-4Zr, respectively, were chosen to be situated inside the single $\alpha$ phase field region. The significant grain growth after the 30 min heat treatments compared to the 1 h heat treatment at 1325°C of Fig. 5a and b is indeed indicative for the presence of this single phase field region. Again, a partial formation of massive $\gamma$ phase could not be prevented during water-quenching at the end of these heat treatments.

Heat treatments in the temperature range close to the peritectic transformation of the respective alloys resulted in the microstructures shown in Fig. 5e and f. The liquid phase formed at grain boundaries and triple points. In particular, a so-called incomplete wetting of the interfaces between the solid grains by the liquid phase occurred during the heat treatments [45,46]. As indicated in Fig. 5, solidification products of the melt can be identified by the bright contrast in the BSE-SEM micrographs. Regarding the grains making up the remaining microstructure, two different types can be observed. Firstly, some grains show a substructure consisting of individual lath-like grains. These structures are a consequence of the $\beta\rightarrow\alpha$ transformation, which is not suppressible during water-quenching and, thus, yields structures similar to the so-called basket-net-weave structures observed in Ti base alloys [47]. Consequently, grains containing such an inner substructure correspond to the high-temperature $\beta$ phase. Secondly, grains with homogeneous BSE contrast are associated with the high-temperature $\alpha$ phase, as this phase only undergoes an ordering into $\alpha_2$ during water-quenching. Furthermore, in some of the grains with a homogeneous BSE contrast, massive $\gamma$ phase can be found, which is a further evidence that they belong to the high-temperature $\alpha$ phase. A further identification characteristic is the difference in the overall BSE contrast of the high-temperature $\alpha$ and $\beta$ phases. The latter phase appears slightly brighter because of a higher Ti content but also due to an enrichment in Zr [10]. A comparison between Fig. 5e and f shows that the amounts of $\beta$ and liquid phases are higher in the Ti-46Al-2Zr alloy than in the Ti-46Al-4Zr alloy meaning that the corresponding heat treatment temperature is situated higher in the $\alpha+\beta+$L phase field region. For the highest heat treatment temperatures, 1470°C for the Ti-46Al-2Zr alloy in Fig. 5g and 1400°C for the Ti-46Al-4Zr alloy in Fig. 5h, all grains belonging to the solid phase present at high temperatures show an inner substructure, because the $\alpha$ phase had already completely dissolved at these temperatures situated within

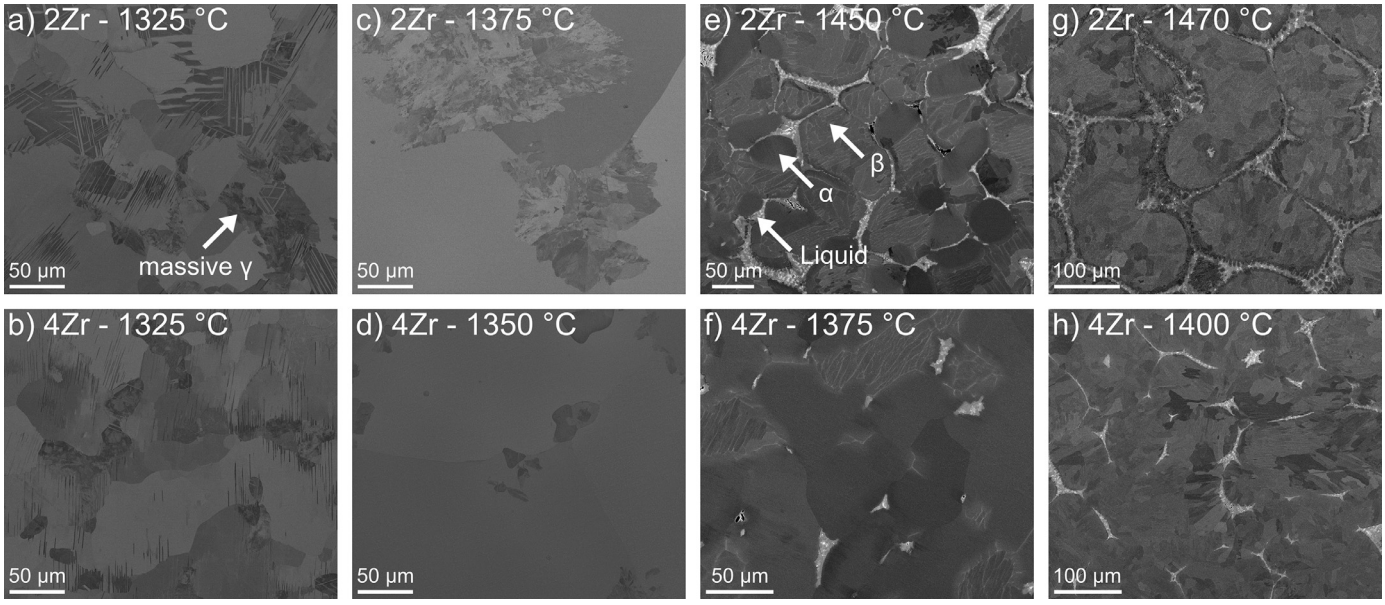


**Fig. 5.** BSE-SEM images of the heat-treated and water-quenched microstructures of the Ti-46Al-2Zr and the Ti-46Al-4Zr alloy. The respective heat treatment temperature is given in each micrograph. The heat treatment duration was 30 min for all temperatures with exception of 1325°C, for which a time of 60 min was used; (a)–(d) and (e)–(h) correspond to temperatures below and above the solidus temperatures of the different alloys, respectively. Examples of microstructural features belonging to the massive $\gamma$ phase as well as to the high-temperature $\alpha$, $\beta$ and liquid phase are marked in (a) and (e).

the $\beta$+L phase field region. Furthermore, the fraction of wetted grain boundaries increases with heat treatment temperature and Zr content of the alloy, because both parameters bring the material closer to the stability region of the liquid phase. For example, in the case of Fig. 5g, the grain boundaries of the former $\beta$ grains have been almost completely wetted by the liquid phase. However, any influence of the grain boundary wetting on the observed phase equilibria can be excluded, since it may only affect the microstructural appearance but not the phases present. Finally, these microstructures of the heat-treated samples corroborate the findings of the HEXRD and DSC measurements.

A more detailed investigation of the microstructure above the solidus temperature was conducted for the Ti-46Al-4Zr alloy heat-treated at 1400 °C for 30 min followed by water-quenching (Fig. 5h). Fig. 6 shows a part of the microstructure characterized by EBSD and EDX. The EBSD analysis confirms that the high-temperature $\beta$ phase transforms into $\alpha$, and subsequently $\alpha_2$, during water-quenching, which results in a lath-like substructure within the former $\beta$ grains (green areas in Fig. 6). Interestingly, the parts of the microstructure, which correspond to the liquid phase at the heat treatment temperature, consist solely of $\gamma$ phase (blue area in Fig. 6). The EDX results in Fig. 6 reveal that the prior liquid phase is enriched in Al and Zr, while being depleted in Ti when compared with the high-temperature $\beta$ phase. Concerning Ti and Al, this can be explained by the fact that the point in the peritectic triangle adjoined to the single liquid phase field region is situated at the Al-rich side in the Ti-Al system. As the high cooling rate of the water-quenching prohibits long-range diffusion processes, the overall chemical composition of the liquid stays almost constant during cooling, which causes a solidification resulting in only $\gamma$ phase. With respect to Zr, the amount in the high-temperature $\beta$ phase is about 3.9 at.% and in the liquid about 9.4 at.%. This yields a partition coefficient $k(L/\beta)$ of about 2.4 ± 0.15 and shows that this element rather partitions into the liquid phase than into the $\beta$ phase at high temperatures. Furthermore, local chemical segregations due to a dendritic solidification are present within the $\gamma$ phase, as indicated in Fig. 6 by the composition-sensitive BSE signal of this phase which is superimposed with the EBSD data.

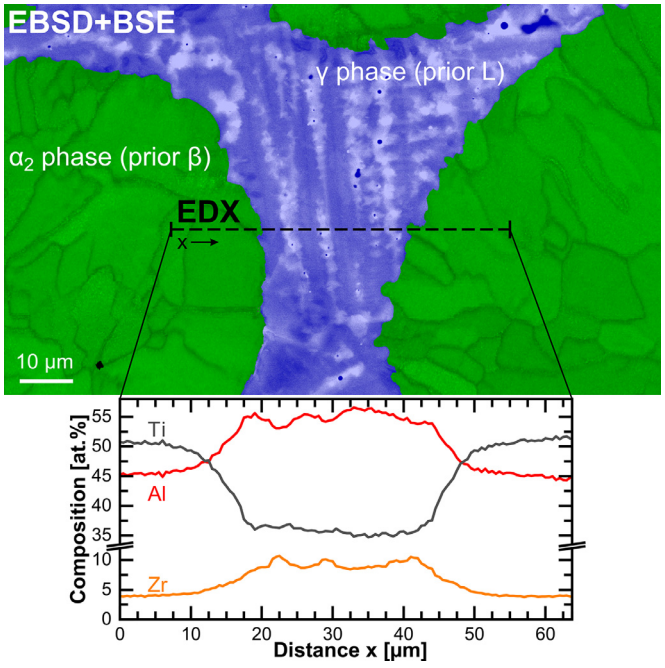


**Fig. 6.** EBSD phase map of the Ti-46Al-4Zr alloy heat-treated at 1400°C for 30 min showing $\alpha_2$ phase (green) and $\gamma$ phase (blue), which formed during water-quenching from the high-temperature $\beta$ phase and liquid phase (indicated in parentheses), respectively. The EBSD signal of the $\gamma$ phase is superimposed with the corresponding BSE signal to visualize the chemical differences (see text). Additionally, the results of an EDX line scan highlighting the quantitative changes of Ti, Al and Zr are presented.

The interdendritic areas, corresponding to the last solidifying liquid phase, appear brighter in the BSE contrast. The elemental distribution in Fig. 6 shows that these areas possess an even higher Zr content than the remainder of the $\gamma$ phase, e.g. two small peaks are observable in the Zr curve between 20 and 30 µm along the EDX measurement line.

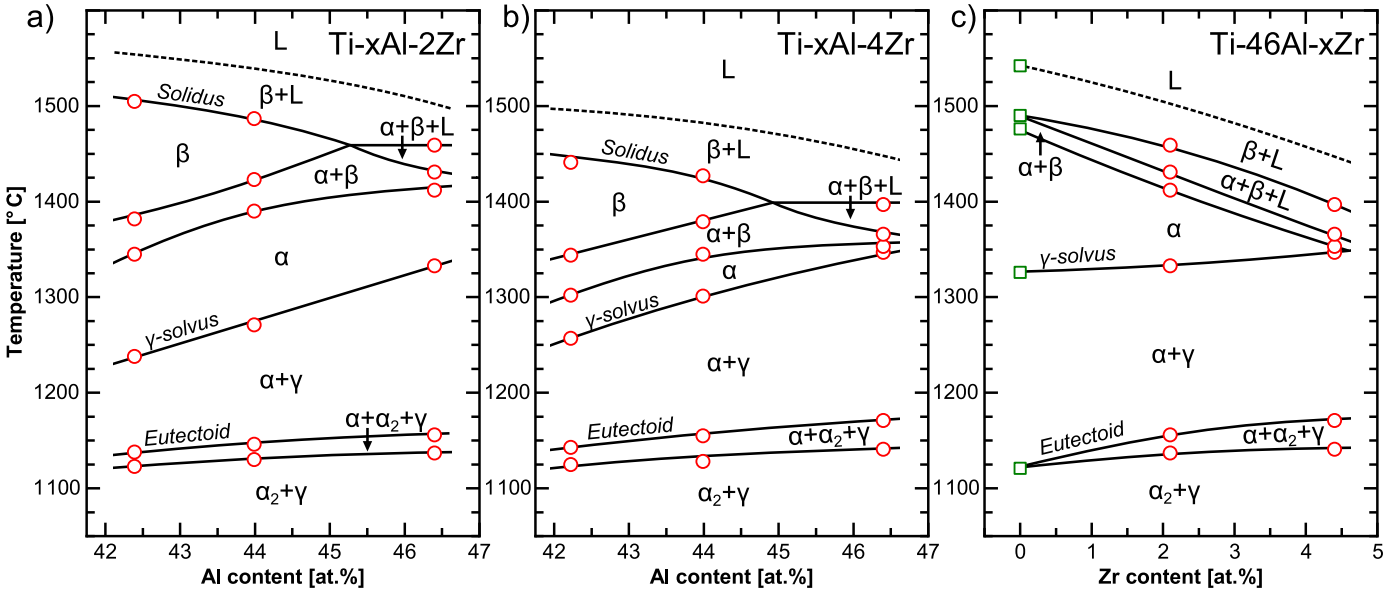


**Fig. 7.** Experimentally determined quasi-binary Ti-xAl-2Zr, Ti-xAl-4Zr and Ti-46Al-xZr isopleths. Important phase transition temperatures, i.e. $\gamma$-solvus, eutectoid and solidus, are individually marked. The green rectangles correspond to the results of CALPHAD calculations for a binary Ti-46Al (at.%) alloy using the software Thermo-Calc. The liquidus temperatures (dashed lines) were taken from Ref. [35].

### 3.4. Influence of Zr on the Ti-Al phase diagram

By combining the results of the DSC and HEXRD investigations with the observations derived from the heat-treated samples, certain isopleths of the Ti-Al-Zr system were experimentally assessed for the investigated composition range. Fig. 7a and b show the quasi-binary sections of the Ti-Al-Zr phase diagram for Zr contents of 2 at.% and 4 at.% in dependence on the Al content. In addition, Fig. 7c presents the Ti-46Al-xZr isopleth. Thermodynamic calculations were carried out using the software Thermo-Calc to determine the transformation temperatures of the binary Ti-46Al composition (green squares in Fig. 7c), as it is well covered by the current data base. The liquidus temperatures were derived from the work of Wang et al. [35].

Starting from low temperatures, Zr increases the eutectoid temperature and, thus, stabilizes the ordered $\alpha_2$ phase over its disordered counterpart. Similar behaviour has also been reported in literature for other alloying elements in $\gamma$-TiAl based alloys, e.g. the $\beta$-stabilizing elements Nb, Mo and V [41,48,49]. In the binary Ti-Al system, the eutectoid transformation, equivalent to the $\alpha_2 \leftrightarrow \alpha$ order/disorder reaction, happens at one defined temperature independent of the Al content in accordance with the Gibbs phase rule. Additions of a third element morph this eutectoid line into an extended $\alpha+\alpha_2+\gamma$ phase field region, as emphasized in the Ti-46Al-xZr isopleth in shown Fig. 7c. Additionally, raising the Zr content from 2 at.% to 4 at.% yields an increased dependence of the eutectoid temperature from the alloy's Al content. In other words, the Al-induced changes of the eutectoid temperature increase due to Zr additions.

The $\gamma$-solvus temperature, which limits the $\alpha+\gamma$ phase field region from above, is also shifted to higher values due to Zr. In order to quantitatively compare the effect of Zr and Al on this transition temperature, which is crucial for industrial heat treatments to achieve different types of microstructures in $\gamma$-TiAl based alloys, i.e. fully-lamellar or nearly-lamellar [2], the corresponding data points were fitted to the following equation.

$$T_{\gamma-solvus}(x_{Al}, x_{Zr}) = T_0 + c_{Al}(x_{Al} - 42) + c_{Zr}(x_{Zr} - 2) + c_{Al,Zr}(x_{Al} - 42)(x_{Zr} - 2) \quad (1)$$

The parameter $T_0$ corresponds to the $\gamma$-solvus temperature of the alloy with 42 at.% Al and 2 at.% of Zr, i.e. 1238°C. The parameters $c_i$ denote the individual effect of the respective alloying element on the phase transition temperature. Fitting Eq. (1) to the experimental data yields values of $c_{Al}$=21.8°C/at.%, $c_{Zr}$=9.3°C/at.% and $c_{Al,Zr}$=0.4°C/at.%$^2$. The comparison of $c_{Al}$ and $c_{Zr}$ shows that the effect of Zr on the $\gamma$-solvus temperature is less than half of that of Al. Furthermore, the low value of $c_{Al,Zr}$, which essentially describes an interactive effect of these alloying elements, shows that there is no interplay effect of Al and Zr on the $\gamma$-solvus temperature, when compared to the other coefficients.

Besides the increasing eutectoid and $\gamma$-solvus temperature, the major effects of Zr on the Ti-Al phase diagram are observable at higher temperatures. Firstly, the single $\alpha$ phase field region is significantly narrowed for higher Zr contents. Especially, the Ti-46Al-xZr phase diagram suggests that no such phase field region occurs above approximately 4.5 at.% of Zr for this Al content. Theoretically, this must then give rise to an $\alpha+\beta+\gamma$ phase field region to properly connect the $\alpha+\beta$ and the $\alpha+\gamma$ phase field regions. While some reduction of the $\alpha$ phase field is due to the increasing $\gamma$-solvus temperature, the main driving force is a significant shift of phase transformations involving the $\beta$ phase and liquid phase to lower temperatures. Especially, the solidus temperature is greatly reduced due to Zr additions, e.g. from 1490°C for the binary Ti-46Al alloy to 1375°C for the alloy variant containing 4 at.% of Zr.

With respect to the peritectic triangle, i.e. the $\alpha+\beta+$L phase field region, the same argument applies as for the eutectoid transformation described above. Additions of Zr result in the broadening of this phase field region. The left point of this peritectic triangle is situated at around 45 at.% Al in the Ti-xAl-2Zr and Ti-xAl-4Zr isopleths shown in Fig. 7a and b, where it meets the single $\beta$ phase field region. When compared to the binary Ti-Al phase diagram [5], additions of Zr tend to shift this point to lower Al contents, as Zr stabilizes the liquid phase at the expense of the $\beta$ phase. This is also evident from the partition coefficient $k(L/\beta)$, which is significantly greater than unity. The predicted phase transformation pathway of the Ti-46Al-2Zr and the Ti-46Al-4Zr alloy, i.e. the transition $\alpha \rightarrow \alpha+\beta \rightarrow \alpha+\beta+$L upon heating, is also reasonable, as this respective Al content results in the same transition behaviour as for the binary Ti-46Al alloy. As Zr has already been shown to

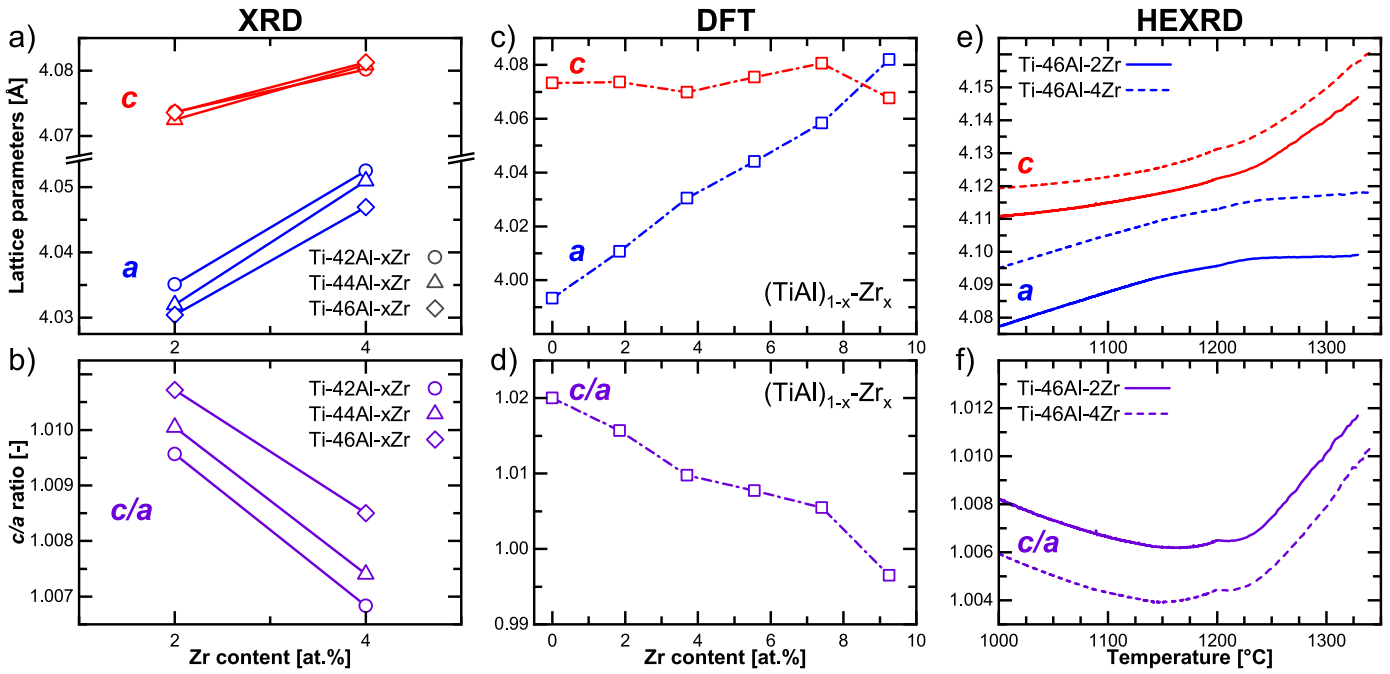


**Fig. 8.** Influence of Al, Zr and temperature on the *a* (blue) and *c* (red) lattice parameter as well as the *c*/*a* ratio (purple) of the $\gamma$ phase determined by XRD (a,b), DFT (c,d) and HEXRD (e,f). In a) and (b) the lattice parameters are presented as a function of the alloy's nominal Al and Zr content, while they are shown in dependence of the Zr content in the $\gamma$ phase in (c) and (d).

favour the existence of the $\beta$ phase over the $\alpha$ phase [10], the formation of small amounts of $\beta$ phase just below the solidus temperature becomes even more plausible. Furthermore, the peritectic point, at which the material transitions directly from the $\alpha$ phase field region into the $\alpha$+$\beta$+L phase field region, can be estimated from the Ti-xAl-2Zr and the Ti-xAl-4Zr isopleth to be approximately situated at around 47 at.% Al.

### 3.5. Influence of Zr on the lattice parameters of the $\gamma$ phase

With respect to the lattice parameters of the $\gamma$ phase, both an increase and a decrease for ternary Ti-Al-Zr alloys with similar compositions are contrarily reported in literature by different authors [7,8]. In the present work, XRD, HEXRD and ab-initio DFT calculations were employed to study concentration- and temperature-induced changes of the lattice parameters *a* and *c* of the $\gamma$ phase in the investigated alloys. The results obtained by these different techniques are summarized in Fig. 8. The corresponding values for *a*, *c* and *c*/*a* determined by XRD in the as-HIPed condition are shown in Fig. 8a and b as a function of the respective alloy's nominal Zr and Al content. This was done because a reliable quantitative EDX measurement of the composition of the $\gamma$ phase was not possible for the as-HIPed condition due to the small lamellar spacing of the $\alpha_2/\gamma$ colonies in the microstructure, e.g. see Fig. 1. However, the chemical composition of the $\gamma$ phase could be determined for samples heat-treated at 1300°C for 1 h because of the associated grain coarsening. Exemplarily, EDX measurements of these heat-treated samples revealed that this phase consisted of 46.5 at.% Al and 2.6 at.% Zr in the Ti-46Al-2Zr and of 45.7 at.% Al and 4.8 at.% Zr in the Ti-46Al-4Zr alloy, giving at least a trend for the composition of the $\gamma$ phase compared to the nominal composition of the alloy in the as-HIPed condition. Consequently, while the Al content of the $\gamma$ phase roughly corresponds to the overall Al content of the alloy, the actual Zr content of this phase is slightly increased in the relevant composition range.

As shown in Fig. 8a, the lattice parameter *c* is essentially independent of the Al content, while a slight decrease of the lattice parameter *a* is induced by higher amounts of Al. Thus, an increase of the *c*/*a* ratio with increasing Al content is observed in Fig. 8b. As described in the work by Yeoh et al. [50], this is attributed to a change in the chemical ordering of the $\gamma$ phase. Because an Al content below its ideal stoichiometry of 50Ti-50Al increases the chemical disorder in the tetragonally distorted crystal structure, the $\gamma$ phase becomes more cubic for lower Al contents. Compared to the effect of Al, the influence of Zr on the lattice parameters of the $\gamma$ phase in the as-HIPed condition is much more pronounced. Fig. 8a shows that Zr increases both the *a* and *c* lattice parameter. Because the lattice parameter *a* is more heavily influenced than *c*, a decrease of the *c*/*a* ratio is observable for increased additions of Zr in the investigated Al range. This is in agreement with the observations reported by Tanda et al. [8] for $\gamma$ single-phase alloys with 50 at.% Al.

The lattice parameters' dependences on the Zr content of the $\gamma$ phase as predicted by ab-initio DFT calculations based on the compositional model $(TiAl)_{1-x}$-$Zr_x$, see Fig. 8c and d, provide essentially the same trends as derived from the XRD measurements. More precisely, the calculated lattice parameter *a* increases significantly upon alloying with Zr, while *c* stays almost constant. The experimental XRD and calculated DFT changes agree even quantitatively, e.g. XRD and DFT show an increase in the lattice parameter *a* of 0.018 Å and 0.021 Å, respectively, when comparing 2 at.% and 4 at.% Zr. For the highest calculated Zr amount of 9.25 at.%, i.e. more than twice the amount as in the experimental alloys, the ab-initio DFT calculations even predict an *c*/*a* ratio below unity.

The different impact of Zr on the lattice parameters of the $\gamma$ phase may be explained by differing interactions with the Ti and the Al atoms. The stoichiometric crystal structure of the $\gamma$ phase can be represented as an alternate stacking of (001) planes consisting only of Ti or Al atoms, respectively, along the direction of the *c* axis. Placing Zr on an Al plane, which can be alternatively termed as placing Zr on the Al sublattice, leads to a strong interaction with neighbouring Ti atoms. This is shown by the occupation of the "out-of-the-plane" $d_{xz}$ and $d_{yz}$ orbitals of Zr (Fig. 9a, middle panel), which interact with the corresponding Ti-orbitals

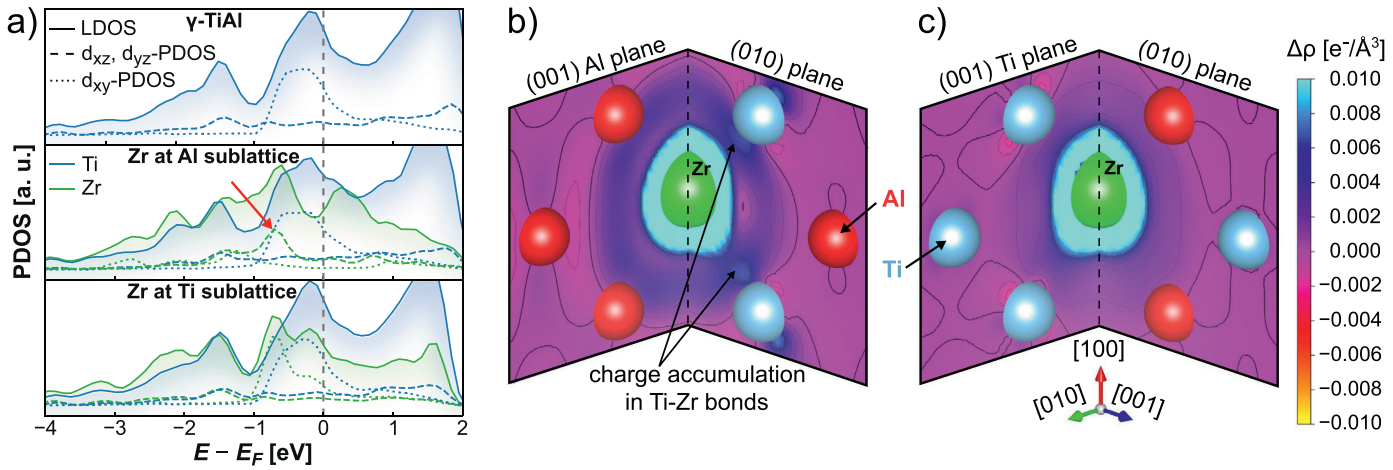


**Fig. 9.** Impact of Zr on the electronic structure of $\gamma$-TiAl. (a) Local (LDOS, solid line) and projected density of states (PDOS, dotted and dashed lines) of Ti (blue) and Zr (green) in perfect $\gamma$-TiAl (upper panel), Zr on Al sublattice (middle panel) and Zr on Ti sublattice (bottom panel). Charge density difference map for (b) Zr on Al sublattice and (c) Zr on Ti sublattice is plotted on two mutually perpendicular planes, (001) which is perpendicular to the *c* lattice vector, and (010) which is along the *b* lattice vector (having the length *a*).

on neighbouring (001) planes. This is incompatible with the occupation of the *d*-orbitals in $\gamma$-TiAl (Fig. 9a, top panel), where the near-to-Fermi level region is dominated by the $d_{xy}$ and $d_{z2}$ orbitals. The latter gives rise to the peak in Ti local density of states (LDOS) just below the Fermi level, and it is completely unoccupied in Zr (local minimum in Zr LDOS). The formation of Ti-Zr $d_{xz}$ orbitals is also visualised by the charge accumulation on the (010) plane in the charge density difference map, see Fig. 9b, showing the difference between the charge distribution in perfect $\gamma$-TiAl and $\gamma$-TiAl with one Zr atom replacing one Al atom. Furthermore, there is a symmetrical charge accumulation in the (001) plane, likely corresponding to some non-bonding Zr *d*-states. On the other hand, when Zr replaces Ti (Zr sits on Ti sublattice), the charge redistribution shown in Fig. 9c corresponds only to more spatially extended valence states of Zr (5*s*4*d*) in comparison to Ti (4s3*d*). Likewise, the DOS (Fig. 9a, bottom panel) suggests occupation of the same type of Zr-*d* orbitals as in the case of Ti in the perfect $\gamma$-TiAl. Overall, this analysis is in line with former reports suggesting that Zr prefers the Ti sublattice in $\gamma$-TiAl [51]. In order to keep the Al and Ti content balanced, addition of Zr leads to a creation of Ti antisites on the Al sublattice, thus, justifying the used structural model $(TiAl)_{1-x}Zr_x$. Since a hypothetical $\gamma$-TiZr structure with all Al atoms replaced by Zr was reported to exhibit a *c*/*a* ratio of ~0.95 [52], it is reasonable to expect that the addition of Zr, leading to formation of Ti antisites, results in a decreasing *c*/*a* ratio.

The temperature dependence of the $\gamma$ lattice parameters and the corresponding *c*/*a* ratio was investigated by means of Rietveld analysis of the diffraction data obtained during the *in situ* heating HEXRD experiments conducted on the Ti-46Al-2Zr and the Ti-46Al-4Zr alloy. The resulting curves for *a*, *c* as well as *c*/*a* are presented in Fig. 8e and f, respectively. Firstly, the alloys of different Zr content maintain the same qualitative behaviour regarding $\gamma$ as described above irrespective of the temperature: an increase of *a* and *c* and a decrease of the *c*/*a* ratio with increasing Zr content. Secondly, while both lattice parameters continuously increase due to thermal expansion, see Fig. 8e, the *c*/*a* ratio shows a local minimum in the region between 1150°C and 1175°C. Note that the small peak at 1200°C in the *c*/*a* ratio curves in Fig. 8f is related to the change of the heating rate during the *in situ* heating HEXRD experiments and is, therefore, to be regarded only as a measurement artefact. The particular temperature-induced behaviour, though, can be attributed to changes in the chemical composition of the $\gamma$ phase. As the material transitions through the $\alpha+\gamma$ phase field region towards the $\gamma$-solvus temperature upon heating, the Al content of the $\gamma$ phase increases in accordance with the phase diagram [5]. Consequently, as already discussed for the XRD measurements above, this increasing Al content causes an increasing *c*/*a* ratio for higher temperatures, because the phase composition moves towards the ideal stoichiometry [50]. The minimum of the *c*/*a* ratio at approximately 1150°C is explained by the fact, that at around this temperature, i.e. the eutectoid temperature, the Al content of the $\gamma$ phase exhibits a local minimum [5].

## 4. Conclusions

In the present work, six model alloys based on the Ti-(42-46)Al (at.%) system were investigated with respect to the influence of additions of 2 at.% and 4 at.% of Zr on the appearing microstructures as well as on the occurring phase transformations. After the HIP treatment, the alloys predominantly consist of $\alpha_2/\gamma$ colonies as well as of small amounts of globular $\gamma$ phase. Zirconium was found to increase, on the one hand, the amount of the $\gamma$ phase at the expense of the $\alpha_2$ phase in the microstructure and, on the other hand, the material's hardness due to solid solution strengthening and refinement of the lamellae spacing inside the colonies. DSC measurements clearly pointed towards an increase of the eutectoid and $\gamma$-solvus temperature with increasing Zr content, while phase transformations at higher temperatures, especially those involving the liquid phase, were shifted to lower temperatures. These findings were confirmed by *in situ* HEXRD experiments conducted on the Ti-46Al-2Zr (at.%) and Ti-46Al-4Zr (at.%) alloys, which further revealed the presence of a small $\alpha+\beta$ phase field region before transition into the peritectic $\alpha+\beta+L$ phase field region takes place for the respective Al and Zr contents. Consequently, both compositions are situated at the Al-lean side of the peritectic point in the Ti-Al-Zr phase diagram. Generally, Zr drastically decreases the material's solidus temperature and, thus, effectively narrows the single $\alpha$ phase field region. During heat treatments above the solidus temperature in the peritectic phase field region, Zr predominately partitions to the liquid phase followed by the $\beta$ and the $\alpha$ phase. The high cooling rate of water-quenching after the heat treatments results in the transformation of the liquid and the $\beta$ phase into $\gamma$ and $\alpha_2$, respectively. Furthermore, by employing XRD and ab-initio DFT calculations Zr was found to strongly reduce the *c*/*a* ratio of the $\gamma$ phase due to an asymmetric influence on the lattice param-

**Table A.1**
Phase transformation temperatures in °C of the investigated alloys as determined by different experimental techniques. In case of the alloy variants with 46 at.% Al, the two different values for each transition temperature correspond to the DSC (first value) and *in situ* HEXRD measurements (second value), respectively. For the other alloys, the given temperatures were determined by DSC.

| Alloy | $\alpha_2 \rightarrow \alpha$-start | $\alpha_2 \rightarrow \alpha$-end | $\gamma$-solvus | $\alpha+\beta$-transus | $\beta$-transus | $\alpha+\beta$+L-transus | $\beta$+L-transus |
|---|---|---|---|---|---|---|---|
| Ti-42Al-2Zr | 1123 | 1138 | 1238 | 1345 | 1382 | n.a. | 1505 |
| Ti-42Al-4Zr | 1125 | 1143 | 1257 | 1302 | 1344 | n.a. | 1441 |
| Ti-44Al-2Zr | 1130 | 1146 | 1271 | 1390 | 1423 | n.a. | 1487 |
| Ti-44Al-4Zr | 1128 | 1155 | 1301 | 1345 | 1379 | n.a. | 1427 |
| Ti-46Al-2Zr | 1137/1130 | 1156/1148 | 1330/1331 | 1412/1409 | n.a. | 1429/1431 | 1459/1462 |
| Ti-46Al-4Zr | 1141/1133 | 1171/1167 | 1348/1346 | n.d./1353 | n.a. | n.d./1366 | 1398/1396 |

Abbreviations: n.a. = not applicable; n.d. = not detectable with the used experimental technique.

eters, i.e. a significant elongation of the *a* axis, while the *c* axis is mostly unaffected.

## Declaration of Competing Interest

The authors declare that they have no known competing financial interests or personal relationships that could have appeared to influence the work reported in this paper.

## Acknowledgments

Michael Musi is a Recipient of a DOC Fellowship of the Austrian Academy of Sciences at the Department of Materials Science, Montanuniversität Leoben. We acknowledge DESY (Hamburg, Germany), a member of the Helmholtz Association HGF, for the provision of experimental facilities. Parts of this research were carried out at PETRA III and we would like to thank Dr. Norbert Schell for assistance in using beamline P07. Beamtime was allocated for proposal I-20210846 EC. The research leading to this result has been supported by the project CALIPSOplus under the Grant Agreement 730872 from the EU Framework Programme for Research and Innovation HORIZON 2020. The computational results presented have been achieved in part using the Vienna Scientific Cluster (VSC).

## Appendix

A summary of the phase transformation temperatures determined by DSC and HEXRD for the investigated alloys in the Ti-(42-46)Al-(2-4)Zr (at.%) system is shown in Table A.1. The DSC values were determined by a linear extrapolation to a heating rate of 0°C/min. The temperatures determined by HEXRD correspond to a heating rate of 2°C/min below 1200°C and 20°C/min for higher temperatures.

## References

[1] B.P. Bewlay, S. Nag, A. Suzuki, M.J. Weimer, TiAl alloys in commercial aircraft engines, Mater. High Temp. 33 (2016) 549–559.
[2] H. Clemens, S. Mayer, Design, processing, microstructure, properties, and applications of advanced intermetallic TiAl alloys, Adv. Eng. Mater. 15 (2013) 191–215.
[3] S. Mayer, P. Erdely, F.D. Fischer, D. Holec, M. Kastenhuber, T. Klein, H. Clemens, Intermetallic $\beta$-solidifying $\gamma$-TiAl based alloys – From fundamental research to application, Adv. Eng. Mater. 19 (2017) 1600735.
[4] F. Appel, J.D.H. Paul, M. Oehring, Gamma Titanium Aluminides - Science and Technology, WILEY-VCH, Weinheim, 2011.
[5] J.C. Schuster, M. Palm, Reassessment of the binary aluminum-titanium phase diagram, J. Phase Equilib. Diffus. 27 (2006) 255–277.
[6] A. Couret, J.P. Monchoux, D. Caillard, On the high creep strength of the W containing IRIS-TiAl alloy at 850°C, Acta Mater. 181 (2019) 331–341.
[7] T. Kawabata, H. Fukai, O. Izumi, Effect of ternary additions on mechanical properties of TiAl, Acta Mater. 46 (1998).
[8] D. Tanda, T. Tanabe, R. Tamura, S. Takeuchi, Synthesis of ternary $L1_0$ compounds of Ti–Al–Zr system and their mechanical properties, Mater. Sci. Eng. A 387-389 (2004) 991–995.
[9] V.M. Imayev, A.A. Ganeev, D.M. Trofimov, N. Parkhimovich, R.M. Imayev, Effect of Nb, Zr and Zr + Hf on the microstructure and mechanical properties of $\beta$-solidifying $\gamma$-TiAl alloys, Mater. Sci. Eng. A 817 (2021) 141388.
[10] R. Kainuma, Y. Fujita, H. Mitsui, I. Ohnuma, K. Ishida, Phase equilibria among $\alpha$ (hcp), $\beta$ (bcc) and $\gamma$ ($L1_0$) phases in Ti-Al base ternary alloys, Intermetallics 8 (2000) 855–867.
[11] F. Yang, F.H. Xiao, S.G. Liu, S.S. Dong, L.H. Huang, Q. Chen, G.M. Cai, H.S. Liu, Z. Jin, Isothermal section of Al–Ti–Zr ternary system at 1273K, J. Alloy. Compd. 585 (2014) 325–330.
[12] S. Neumeier, J. Bresler, C. Zenk, L. Haußmann, A. Stark, F. Pyczak, M. Goeken, Partitioning behavior of Nb, Ta, and Zr in fully lamellar $\gamma/\alpha_2$ titanium aluminides and its effect on the lattice misfit and creep behavior, Adv. Eng. Mater. 23 (2021) 2100156.
[13] V.M. Imayev, N.Y. Parkhimovich, D.M. Trofimov, R.M. Imayev, Effect of Nb, Zr and Zr+Hf on the lattice parameters of the intermetallic phases and creep behavior of $\gamma$-TiAl alloys based on Ti-44Al-0.2B, Lett. Mater. 11 (2021) 524–530.
[14] M.A. Turchanin, P.G. Agraval, A.R. Abdulov, Thermodynamic assessment of the Cu-Ti-Zr system. II. Cu-Zr and Ti-Zr systems, Powder Metall. Met. Ceram. 47 (2008) 428–446.
[15] E. Fischer, C. Colinet, An updated thermodynamic modeling of the Al-Zr system, J. Phase Equilib. Diffus. 36 (2015) 404–413.
[16] D.A. Abreu, A. Silva, J. Santos, D.F. Barros, C.S. Barros, N. Chaia, C.A. Nunes, G.C. Coelho, Liquidus projection of the Al–Ti–Zr system, J. Alloy. Compd. 849 (2020) 156463.
[17] K. Lü, F. Yang, Z. Xie, H. Liu, G. Cai, Z. Jin, Isothermal section of Al–Ti–Zr ternary system at 1073 K, Trans. Nonferrous Met. Soc. China 26 (2016) 3052–3058.
[18] Z. Kahrobaee, M. Palm, Critical assessment of the Al-Ti-Zr system, J. Phase Equilib. Diffus. 41 (2020) 687–701.
[19] J. Bresler, S. Neumeier, M. Ziener, F. Pyczak, M. Goeken, The influence of niobium, tantalum and zirconium on the microstructure and creep strength of fully lamellar $\gamma/\alpha_2$ titanium aluminides, Mater. Sci. Eng. A 744 (2019) 46–53.
[20] P. Staron, T. Fischer, T. Lippmann, A. Stark, S. Daneshpour, D. Schnubel, E. Uhlmann, R. Gerstenberger, B. Camin, W. Reimers, E. Eidenberger, H. Clemens, N. Huber, A. Schreyer, *In situ* experiments with synchrotron high-energy X-rays and neutrons, Adv. Eng. Mater. 13 (2011) 658–663.
[21] M. Musi, B. Galy, J.P. Monchoux, A. Couret, H. Clemens, S. Mayer, *In-situ* observation of the phase evolution during an electromagnetic-assisted sintering experiment of an intermetallic $\gamma$-TiAl based alloy, Scr. Mater. 206 (2022) 114233.
[22] A.P. Hammersley, S.O. Svensson, M. Hanfland, A.N. Fitch, D. Hausermann, Two-dimensional detector software: from real detector to idealised image or two-theta scan, High Pressure Res 14 (1996) 235–248.
[23] L. Lutterotti, Total pattern fitting for the combined size–strain–stress–texture determination in thin film diffraction, Nucl. Instrum. Meth. B 268 (2010) 334–340.
[24] C. Fleissner-Rieger, T. Pogrielz, D. Obersteiner, T. Pfeifer, H. Clemens, S. Mayer, An additively manufactured titanium alloy in the focus of metallography, Pract. Metallogr. 58 (2021) 4–31.
[25] P. Hohenberg, W. Kohn, Inhomogeneous electron gas, Phys. Rev. 136 (1964) B864–B871.
[26] W. Kohn, L.J. Sham, Self-consistent equations including exchange and correlation effects, Phys. Rev. 140 (1965) A1133–A1138.
[27] G. Kresse, J. Furthmueller, Efficient iterative schemes for ab initio total-energy calculations using a plane-wave basis set, Phys. Rev. B 54 (1996) 11169–11186.
[28] G. Kresse, J. Furthmueller, Efficiency of ab-initio total energy calculations for metals and semiconductors using a plane-wave set, Comp. Mater. Sci. 6 (1996) 15–50.
[29] G. Kresse, D. Joubert, From ultrasoft pseudopotentials to the projector augmented-wave method, Phys. Rev. B 59 (1999) 1758–1775.
[30] J.P. Perdew, K. Burke, M. Ernzerhof, Generalized gradient approximation made simple, Phys. Rev. Lett. 77 (1996) 3865–3868.
[31] D. Noeger, Optimised structural models of solid solutions for tensorial properties. Master's thesis, Leoben, 2017.
[32] H. Clemens, W. Wallgram, S. Kremmer, V. Guether, A. Otto, A. Bartels, Design of novel $\beta$-solidifying TiAl alloys with adjustable $\beta$/B2-phase fraction and excellent hot-workability, Adv. Eng. Mater. 10 (2008) 707–713.
[33] J.C. Slater, Atomic radii in crystals, J. Chem. Phys. 41 (1964) 3199–3204.
[34] Y. Mishin, C. Herzig, Diffusion in the Ti-Al system, Acta Mater. 48 (2000) 589–623.
[35] J. Wang, W. Zheng, G. Xu, X. Zeng, Y. Cui, Thermodynamic assessment of the Ti–Al–Zr system and atomic mobility of its bcc phase, Calphad 70 (2020) 101801.

[36] J.D.H. Paul, F. Appel, R. Wagner, The compression behaviour of niobium alloyed $\gamma$-titanium aluminides, Acta Mater. 46 (1998) 1075–1085.
[37] E. Schwaighofer, H. Clemens, S. Mayer, J. Lindemann, J. Klose, W. Smarsly, V. Güther, Microstructural design and mechanical properties of a cast and heat-treated intermetallic multi-phase $\gamma$-TiAl based alloy, Intermetallics 44 (2014) 128–140.
[38] G. Hoehne, W.F. Hemminger, H.J. Flammersheim, Differential Scanning Calorimetry, 2nd ed., Springer-Verlag Berlin Heidelberg, New York.
[39] A.T. Dinsdale, SGTE data for pure elements, Calphad 15 (1991) 317–425.
[40] P. Spoerk-Erdely, P. Staron, J. Liu, N. Kashaev, A. Stark, K. Hauschildt, E. Maawad, S. Mayer, H. Clemens, Exploring structural changes, manufacturing, joining, and repair of intermetallic $\gamma$-TiAl-based alloys: Recent progress enabled by *in situ* synchrotron X-ray techniques, Adv. Eng. Mater. 23 (2021) 2000947.
[41] M. Musi, H. Clemens, A. Stark, P. Staron, P. Spoerk-Erdely, Phase transformations and phase stability in the Ti–44 at.%Al–(0–7 at.%)Mo system, Intermetallics 143 (2022) 107484.
[42] T. Schmoelzer, K.D. Liss, G.A. Zickler, I.J. Watson, L.M. Droessler, W. Wallgram, T. Buslaps, A. Studer, H. Clemens, Phase fractions, transition and ordering temperatures in TiAl–Nb–Mo alloys: an in- and *ex-situ* study, Intermetallics 18 (2010) 1544–1552.
[43] E. Schwaighofer, B. Rashkova, H. Clemens, A. Stark, S. Mayer, Effect of carbon addition on solidification behavior, phase evolution and creep properties of an intermetallic $\beta$-stabilized $\gamma$-TiAl based alloy, Intermetallics 46 (2014) 173–184.
[44] K.D. Liss, A. Bartels, H. Clemens, S. Bystrzanowski, A. Stark, T. Buslaps, F.P. Schimansky, R. Gerling, C. Scheu, A. Schreyer, Recrystallization and phase transitions in a $\gamma$-TiAl-based alloy as observed by *ex situ* and *in situ* high-energy X-ray diffraction, Acta Mater. 54 (2006) 3721–3735.
[45] B.B. Straumal, A. Korneva, A. Kuzmin, G.A. Lopez, E. Rabkin, A.B. Straumal, G. Gerstein, A.S. Gornakova, The grain boundary wetting phenomena in the Ti-containing high-entropy alloys: a review, Metals 11 (2021) 1881.
[46] A.S. Gornakova, S.I. Prokofiev, K.I. Kolesnikova, B.B. Straumal, Formation regularities of grain-boundary interlayers of the $\alpha$-Ti phase in binary titanium alloys, Russ. J. Non-Ferrous Met. 57 (2016) 229–235.
[47] G. Luetjering, J.C. Williams, Titanium, Springer-Verlag Berlin Heidelberg, Germany, 2007.
[48] M. Takeyama, S. Kobayashi, Physical metallurgy for wrought gamma titanium aluminides, Intermetallics 13 (2005) 993–999.
[49] H.F. Chladil, H. Clemens, H. Leitner, A. Bartels, R. Gerling, F.P. Schimansky, S. Kremmer, Phase transformations in high niobium and carbon containing $\gamma$-TiAl based alloys, Intermetallics 14 (2006) 1194–1198.
[50] L.A. Yeoh, K.D. Liss, A. Bartels, H.F. Chladil, M. Avdeev, H. Clemens, R. Gerling, T. Buslaps, *In situ* high-energy X-ray diffraction study and quantitative phase analysis in the $\alpha+\gamma$ phase field of titanium aluminides, Scr. Mater. 57 (2007) 1145–1148.
[51] D. Holec, R.K. Reddy, T. Klein, H. Clemens, Preferential site occupancy of alloying elements in TiAl-based phases, J. Appl. Phys. 119 (2016) 205104.
[52] The Materials Project, ZrTi structure, materialsproject.org/materials/mp-1215236/ (accessed 08.06.2022).